Polymer Journal (2019) 51:895–904
https://doi.org/10.1038/s41428-019-0197-0

ORIGINAL ARTICLE

A diketopyrrolopyrrole-based nonfullerene acceptor for organic solar cells with a high open-circuit voltage of 1.17 V

Zhitian Liu[1] · Di Zeng[1] · Chengjun Gu[1,2] · Jing Wen[3] · Xianbao Duan[1,4] · Qi Zhang[1] · Jie Min[2] · Xiang Gao[1]

Received: 30 January 2019 / Revised: 8 March 2019 / Accepted: 27 March 2019 / Published online: 26 April 2019

Abstract

A new nonfullerene electron acceptor, BP(DPPB)$_4$, with a biphenyl core and four diketopyrrolopyrrole (DPP) arms is synthesized. The molecular geometries, energy levels, optical properties, and photovoltaic properties of the acceptor are systematically studied. The relationship between thermal annealing temperature and morphology formation is discussed. Poly(3-hexylthiophene) is chosen as the electron donor material because of its complementary absorption profile and matched energy levels. The optimized organic solar cells can provide a power conversion efficiency of 1.43% with a high open-circuit voltage (V_{oc}) of 1.17 V after thermal annealing at 120 °C for 10 min.

Introduction

In the past few years, bulk heterojunction (BHJ) polymer solar cells (PSCs) have drawn great attention because of their unique merits, such as light weight, flexibility, low cost, and easy processing [1–3]. The power conversion efficiencies (PCEs) of BHJ PSCs have recently exceeded 15% [4]. In the early stage, high-efficiency BHJ PSCs consisted of narrow bandgap polymer donors with soluble fullerene acceptors, namely, [6,6]-phenyl-C61-butyric acid methyl ester (PC61BM) and its C71 analog (PC71BM), owing to their isotropic electron-transporting capacity, high electron mobility, and ability to induce nanoscale phase separation [5, 6]. However, these fullerene acceptors are relatively expensive, and there are some intrinsic shortcomings of fullerene materials, for instance, limited chemical and energetic tunability, narrow absorption spectra, and morphological instability [7, 8]. Therefore, it is necessary to develop new acceptor materials to solve these problems. Nonfullerene acceptors (NFAs), including small-molecule acceptors [9, 10] and polymeric acceptors [11–14], which have the advantages of broader and stronger absorb spectra, tunable energy levels and lower cost, have drawn increasing attention in recent years.

Small-molecule NFAs exhibit good reproducibility because of their exact molecular structure and high purity. Therefore, at present, much more efforts are devoted to developing small-molecule NFAs than polymeric NFAs [15–17]. Diketopyrrolopyrrole (DPP) dyes have several attractive properties: strong light absorption, good photochemical stability, facile synthetic modification, and high electron mobilities [18–20]. Therefore, some DPP-based materials have been recently developed as acceptors for PSCs. However, not only simple linear DPP-based materials [21–24] but also three-dimensional (3D) DPP-based acceptors [25–27] provided relatively lower PCEs than those of other acceptors when blended with poly(3-hexylthiophene) (P3HT) as donors in BHJ devices. Chen et al. achieved the highest PCE of 5.16% when SF(DPPB)$_4$ with a spirofluorene (SF) core was used as an acceptor and P3HT was used as a donor [27]. Recently, Jun-Hua Wan et al. reported that three NFAs that also had an SF core, SF (DPP3F)$_4$, SF-(DPPBT)$_4$ and SF-(DPPBF)$_4$ [28], yielded

Supplementary information The online version of this article (https://doi.org/10.1038/s41428-019-0197-0) contains supplementary material, which is available to authorized users.

✉ Xiang Gao
xgao@wit.edu.cn

1 Institute of Materials for Optoelectronics and New Energy, School of Material Science & Engineering, Wuhan Institute of Technology, 430073 Wuhan, PR China

2 The Institute for Advanced Studies, Wuhan University, 430073 Wuhan, China

3 School of Chemistry and Chemical Engineering, Nanjing University, 210023 Nanjing, PR China

4 School of Material Science & Engineering, Huazhong University of Science and Technology, 430073 Wuhan, China

moderate PCE values (≤ 2%) when blended with P3HT. It is not hard to observe that most of the attention has been paid to the orthogonal SF core, which is owing to its ability to decrease the crystallinity of DPP dyes, to improve phase separation when blended with P3HT [27] and to enhance multidimensional charge-transporting capacities in the quasi-3D configuration. In our former studies, we used a rotary biphenyl (BP) core to displace the SF in 3D NFAs based on perylene diimides (PDI). The BP core is much cheaper than SF [29], and the photovoltaic performance of BP–PDI_4 using BP as the core outperforms that of NFAs using SF or phenyl as the core unit. The BP core can not only take advantage of the quasi-3D configuration but also result in a smaller aggregation tendency, which is also favorable for better device performance when blended with suitable donors [15].

In this study, a new nonfullerene electron acceptor, BP $(DPPB)_4$, was designed and synthesized via the replacement of the SF core in $SF(DPPB)_4$ with a BP core. The optical, thermal, and photovoltaic properties of $BP(DPPB)_4$ were well characterized. After optimizing the thermal annealing conditions, PSCs based on P3HT and $BP(DPPB)_4$ can achieve a moderate PCE of 1.43%, with a high open-circuit voltage (V_{oc}) of 1.17 V, indicating that BP is a potential candidate to replace SF in constructing multidimensional NFAs.

Experimental section

Instruments

^{1}H-NMR spectra were measured on a Bruker AVANCE 400 MHz NMR (Billerica, MA, USA) spectrometer. Mass spectra were recorded on a Bruker BIFLEX III MALDI-TOF mass spectrometer. Thermogravimetric analysis (TGA) measurements were carried out on a PerkinElmer thermal analysis apparatus (Waltham, MA, USA). Differential scanning calorimetry (DSC) measurements were performed using a METTLER differential scanning calorimeter (DSC822e) (Zurich, Switzerland). TGA and DSC measurements were conducted under nitrogen at a heating rate of 10 °C min^{-1}. Absorption spectra were acquired on a PerkinElmer Lambda 35 (Waltham, MA, USA). The cyclic voltammetry (CV) measurements were recorded on a CHI604E electrochemical workstation (Shanghai, China) by using Pt wire as the counter electrode, a glassy carbon electrode as the working electrode, and a Ag/AgCl electrode as the reference electrode in a 0.1 mol L^{-1} tetrabutylammonium hexafluorophosphate (Bu_4NPF_6) solution with a scanning rate of 100 mV s^{-1}, and the potential of the Ag/Ag^+ reference electrode was internally calibrated by using ferrocene/ferrocenium (Fc/Fc^+) as the redox couple. TEM images were recorded by using a JEM-2100/HR TEM (Beijing, China). The current density–voltage (*J*–*V*) characteristics of the devices were measured under AM 1.5 G illumination using a solar simulator (SS-F5-3A, Enli Technology Co., Ltd) (Santa Clara, California, USA). The light intensity was carefully calibrated with a standard silicon reference before every test.

Materials

All the chemicals and solvents used, unless otherwise specified, were purchased from commercial suppliers (J&K, Energy Chemical, Sinopharm Chemical Reagent Co., Ltd) and used without further purification. P3HT was purchased from J&K. The syntheses of 2,5-bis-(2-ethyl-hexyl)−3-(5-bromo-thiophen-2-yl)−6-(5-phenyl-thiophen −2-yl)−2,5-dihydropyrr-olo[3,4-c]pyrrole-1,4-dione (DPPB-Br) (**4**) and 3,5,3',5'-tetrakis(4,4,5,5-tetramethyl-1,3,2-dioxaborolan-2-yl)biphenyl (BP-Bpin4) (**5**) were conducted according to references [29–32].

Synthesis

2,5-diethylhexyl-3,6-dithiophen-2-ylpyrrolo[3,4-c]pyrrole-1,4-dione (1)

^{1}H-NMR (400 MHz, $CDCl_3$, ppm): δ 8.94 (d, 2 H), 7.64 (d, 2 H), 7.27 (d, 2 H), 4.02 (m, 4 H), 1.83 (m, 2 H), 1.36–1.22 (m, 16 H), 0.81 (m, 12 H).

3-(5-bromothiophen-2-yl)−2,5-bis(2-ethylhexyl)−6-(thiophen-2-yl)−2,5-dihydropy- rrolo[3,4-c]pyrrole-1,4-dione (2)

^{1}H-NMR (400 MHz, $CDCl_3$, ppm): δ 8.91 (dd, 1 H), 8.65 (d, 1 H), 7.64 (dd, 1 H), 7.27–7.25 (m, 1 H), 7.20 (d, 1 H), 4.01–3.99 (m, 2 H), 3.98–3.94 (m, 2 H), 1.86–1.80 (m, 2 H), 1.39–1.22 (m, 16 H), 0.91–0.83 (m, 12 H).

2,5-bis(2-ethylhexyl)−3-(5-phenylthiophen-2-yl)−6-(thiophen-2-yl)−2,5-dihydropy- rrolo[3,4-c]pyrrole-1,4-dione (3)

^{1}H-NMR (400 MHz, $CDCl_3$, ppm): δ 8.96 (d, 1 H), 8.92 (d, 1 H), 7.70–7.66 (m, 2 H), 7.64–7.60 (m, 1 H), 7.46–7.25 (m, 5 H), 4.05–4.01 (m, 4 H), 1.98–1.82 (m, 2 H), 1.41–1.24 (m, 16 H), 0.92–0.83 (m, 12 H).

2,5-bis-(2-ethyl-hexyl)−3-(5-bromo-thiophen-2-yl)−6-(5-phenyl-thiophen-2-yl)−2,5-dihydropyrrolo[3,4-c] pyrrole-1,4-dione (4)

^{1}H-NMR (400 MHz, $CDCl_3$, ppm), δ 8.95 (d, 1 H), 8.61 (d, 1 H), 7.67 (d, 2 H), 7.46–7.32 (m, 4 H), 7.19 (d, 1 H),

4.06–3.92 (m, 4 H), 1.94–1.80 (m, 2 H), 1.39–1.21 (m, 16 H), 0.91–0.82 (m, 12 H).

3,5,3′,5′-tetrakis(4,4,5,5-tetramethyl-1,3,2-dioxaborolan-2-yl)biphenyl (5)

^{1}H-NMR (400 MHz, $CDCl_3$, ppm): δ 8.23 (s, 2 H), 8.12 (d, 4 H), 1.38 (s, 48 H).

6,6′,6″,6‴-([1,1′-biphenyl]−3,3′,5,5′-tetrayltetrakis (thiophene-5,2-diyl))tetrakis (2,5-bis(2-ethylhexyl)−3-(5-phenylthiophen-2-yl)−2,5-dihydropyrrolo[3,4-c] pyrrole-1,4-dione) (6) (BP(DPPB)$_4$)

5 (150 mg, 0.23 mmol), **4** (774.75 mg, 1.14 mmol), tetrakis (triphenylphosphine)palladium(0) (21.07 mg, 118.24 μmol), and tetrabutylammonium bromide (100 mg, 0.31 μmol) were added to a three-necked 100 mL round bottom flask under no light. The flask was purged by eight vacuum/nitrogen fill cycles to remove oxygen and fill the flask with nitrogen. K_2CO_3 aqueous solution (2 mol L^{-1}, 4 mL) and toluene (20 mL) were added to the flask. However, all solutions should be blown with nitrogen for 20 min in advance. The mixture was heated to 80 °C and stirred for 4 days. After cooling to room temperature, the reaction solution was washed with water and extracted repeatedly with dichloromethane. The organic layer was combined and dried with anhydrous sodium sulfate. Then, the solvent was removed from the crude product, which was purified by silica gel chromatography with dichloromethane/methanol (150:1, v/v) as the eluent. The product was obtained as magenta powder (261 mg, yield 45%). ^{1}H-NMR (400 MHz, $CDCl_2$, ppm): δ 9.11–9.01 (dr, 8 H), 7.90–7.80 (dr, 6 H), 7.58 (dr, 12 H), 7.37–7.34 (dr, 16 H), 3.94–3.89 (d, 16 H), 1.90 (m, 8 H), 1.38–1.16 (m, 64 H), 0.90–0.74 (m, 48 H). MS spectrum (MALDI, M^+): calculated for $C_{156}H_{178}N_8O_8S_8$: 2549.7, found: 2571.4([M + Na^+]). The elemental analysis: calculated: C (73.49%), H (7.04%), N (4.39%), found: C (73.66%), H (6.81%), N (4.39%) (Supporting information Figure S1 and Table S1).

DFT calculation

DFT calculations were performed at the B3LYP/6-31 g(d,p) level to determine the geometric configurations and then analyze the electronic structures of BP(DPPB)$_4$. All the calculations were performed using Gaussian 09 (version A.01). All *N*-ethylhexyl substituents were replaced with methyl groups to simplify the calculations.

Device fabrication

The PSC devices were fabricated with the following device structure: ITO/PEDOT:PSS/P3HT:BP(DPPB)$_4$/Ca/Al, and the process of specific device fabrication was performed according to references [26–29]. The difference is that for the active layer, a solution of P3HT and BP(DPPB)$_4$ dissolved in chloroform with 2:1 blend weight ratios at a total solid concentration of 15 mg ml^{-1} was spin-cast at 3500 rpm onto the substrates. In addition, the samples were annealed at different annealing temperatures (80 °C, 120 °C, 150 °C) for 10 min. The effective device area was 0.04 cm^2. Device characterization was carried out under an AM 1.5 G solar simulator (SS-F5-3A, Enli Technology Co., Ltd) (Beijing, China) with an intensity of 100 mW cm^{-2}. The charge carrier mobilities of the P3HT:BP(DPPB)$_4$ films were measured using the space-charge-limited current (SCLC) method. Hole-only devices with a structure of ITO/PEDOT:PSS/active layer/MoO_3/Ag and electron-only devices with a structure of ITO/ZnO/active layer/Ca/Al were also fabricated.

Results and discussion

Synthesis and characterization

The synthetic route for BP(DPPB)$_4$ is shown in Scheme 1, and the chemical structures, energy levels of BP(DPPB)$_4$ and P3HT are shown in Fig. 1. BP(DPPB)$_4$ was synthesized via the Suzuki coupling reaction between BP-pin$_4$ and DPPB-Br [27] using Pd(PPh_3)$_4$ as a catalyst in a moderate yield of 45%. BP(DPPB)$_4$ was characterized by proton nuclear magnetic resonance (^{1}H-NMR), mass spectrometry, and elemental analysis. Thermal properties were studied by TGA and DSC. BP(DPPB)$_4$ exhibited excellent thermal stability with a high decomposition temperature (T_d) of 409 °C at 5% weight loss under a nitrogen atmosphere (as shown in Fig. 2a). The DSC traces for this compound showed a glass transition at ca. 120 °C, solid-phase conversion at ca. 175 °C and a melting peak at ca. 246 °C during the heating process, suggesting that BP(DPPB)$_4$ have a certain degree of crystallinity.

Theoretical calculation

To analyze the performance at the molecular level, the optimization of molecular geometries and successive analysis of frontier molecular orbital electron density distributions were calculated by density functional theory (DFT). As shown in Fig. 3a, the local optimal configuration of BP (DPPB)$_4$ was a three-dimensional molecule with an "X" configuration (see energy variations of different possible configurations derived from the connection of DPPB chains, Supporting information Figure S3), and the dihedral angle between the two DPP arms was 57.3°. Furthermore, the dihedral angle between the two benzene planes of the BP

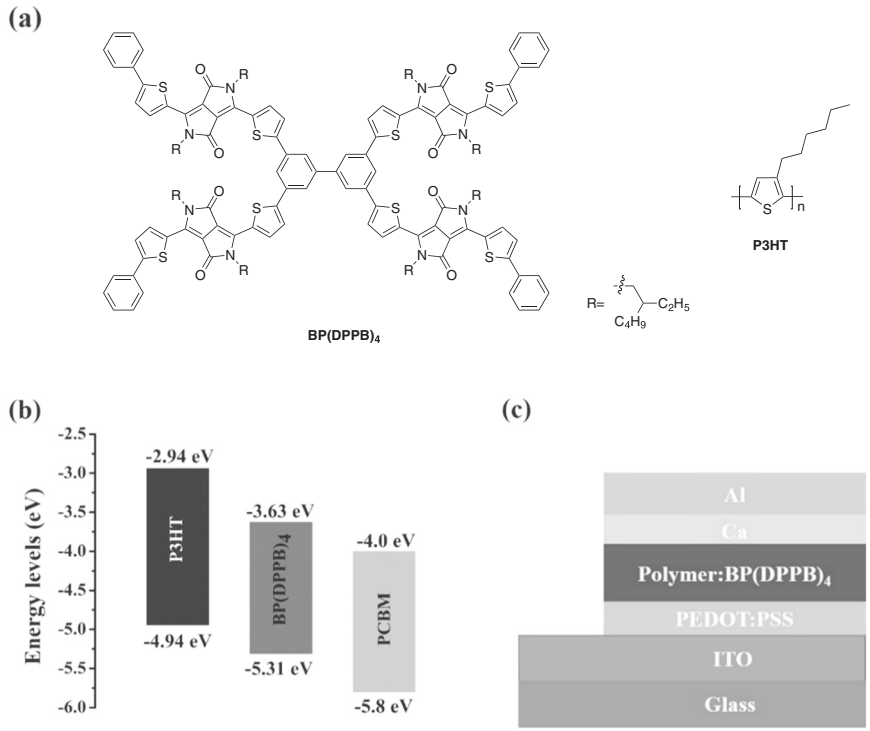

Fig. 1 **a** Chemical structures of $BP(DPPB)_4$ and P3HT; **b** energy level diagram; **c** device structure

core was 143.65°. This molecular configuration can inhibit the strong intermolecular aggregation of $BP(DPPB)_4$. In addition, the two dihedral angles between the two thiophene planes and the DPP building block were 169.47° and 168.34°, and the two dihedral angles between DPP and the two benzene planes, i.e., the benzene group of the BP core and the terminal benzene, were 27.30° and 25.26°, respectively, as shown in Fig. 3b. This result indicates that each arm maintains effective conjugation for photon harvesting and charge transport. Compared with the SF core, the BP core is much smaller in size; additionally, the dihedral angle between the two benzene planes of the BP core is 143.65°, which indicates that the geometry of $BP(DPPB)_4$ is much more compact than that of $SF(DPPB)_4$.

The distributions of the highest occupied molecular orbital (HOMO) and the lowest unoccupied molecular orbital (LUMO) as well as LUMO+1 can also be seen in Fig. 3c and Fig. 3d. The calculated LUMO and LUMO+1 levels are −2.62 eV and −2.59 eV, respectively. The gap between the LUMO and LUMO+1 (ΔLUMO) is 0.03 eV (< 0.5 eV ΔLUMO). The results indicate that $BP(DPPB)_4$ is a highly efficient electron acceptor because the low-lying LUMO+1 may accelerate the charge separation at the interface and induce efficient electron acceptance [33–35].

Optical and electrochemical properties

Figure 4a depicts the molar extinction coefficient of $BP(DPPB)_4$ in $CHCl_3$ solution and the normalized UV spectrum of $BP(DPPB)_4$ in a thin film. $BP(DPPB)_4$ showed two distinct absorption bands, including a weak band in the shorter wavelength region (300–450 nm) and a strong band with a typical aggregation peak in the longer wavelength region (500–700 nm). This spectral profile is well complementary with that of P3HT (400–600 nm), which promotes good light harvesting capability. In solution, the absorption maximum was 607 nm, whereas the absorption maximum in the thin film was 641 nm. This redshift (34 nm) in the maximum absorption peak from the solution to film indicates effective π–π stacking in the thin film. The molar extinction coefficient of $BP(DPPB)_4$ in solution reached up to $2.0 \times 10^5\ \mathrm{M}^{-1}\ \mathrm{cm}^{-1}$, which is beneficial to device performance. Moreover, from the absorption band edges (λ_{onset}, 693 nm) of the $BP(DPPB)_4$ film, the optical band gap (E_g^{opt}) is calculated to be 1.79 eV.

CV measurements were performed to characterize the electrochemical properties of $BP(DPPB)_4$. The LUMO and HOMO energy levels can be estimated from the onset potentials for reduction and oxidation with ferrocene/ferrocenium (Fc/Fc^+) as the internal standard, respectively. The CV curves are shown in Fig. 4, and the date are summarized in Table 1. As shown in Fig. 4b, the onset reduction potential was −1.13 V, and the onset oxidation potential was 0.75 V. Thus, the LUMO level is calculated to be −3.63 eV, and the HOMO level is calculated to be −5.31 eV for $BP(DPPB)_4$. The energy levels are suitable for a high-performance polymer donor (P3HT, as shown in Fig. 1b). The energy offsets (ΔE_{LUMO})

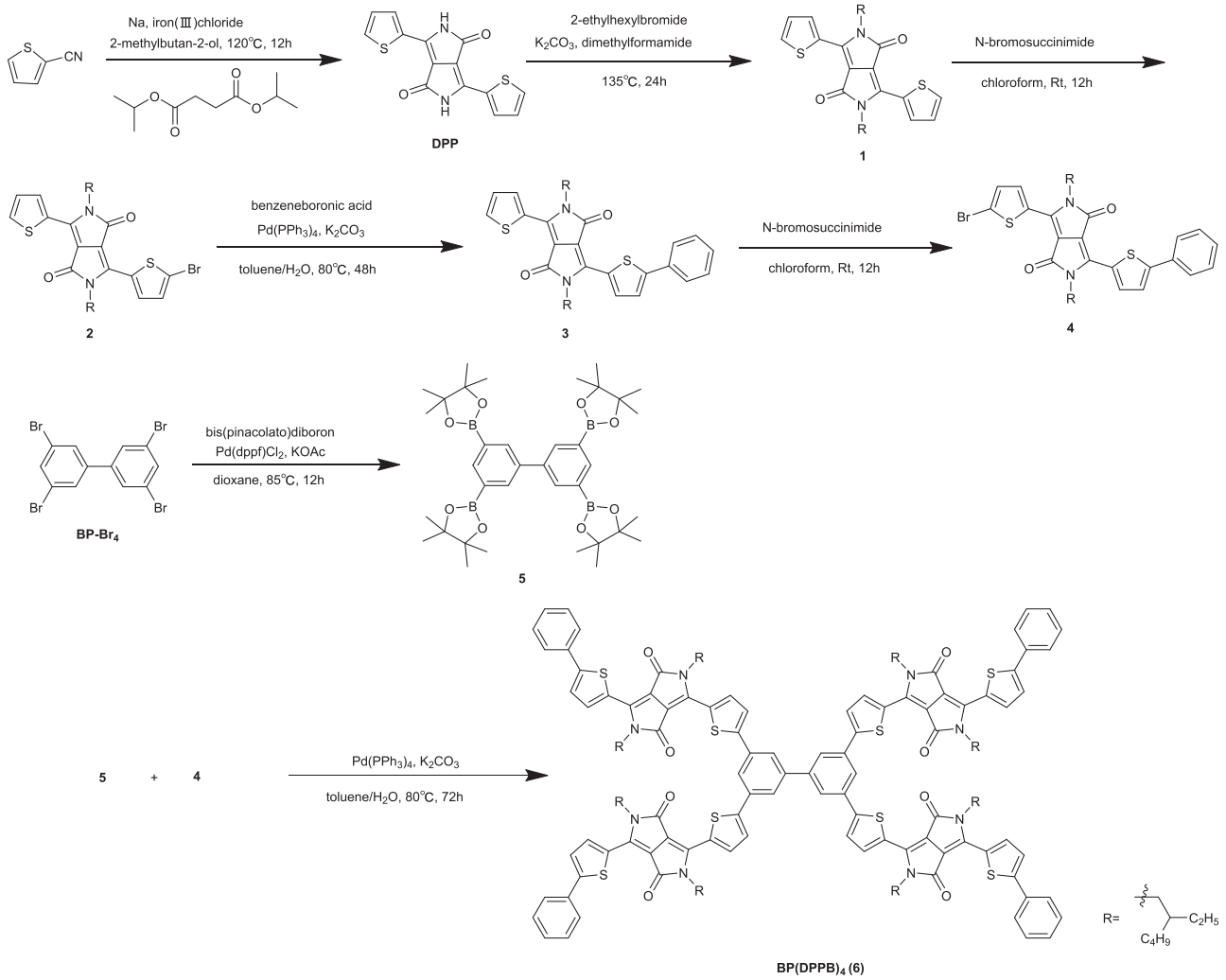

Scheme 1 Synthetic route for BP(DPPB)$_4$

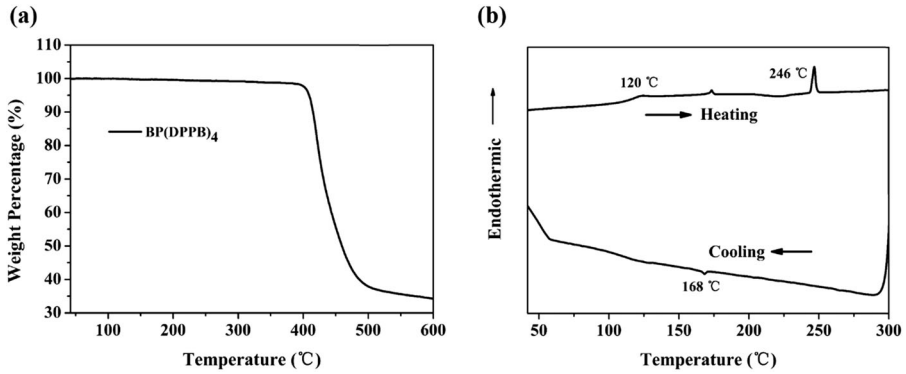

Fig. 2 **a** TGA thermograms of BP(DPPB)$_4$; **b** DSC thermograms of BP(DPPB)$_4$

between the LUMO of P3HT and that of BP(DPPB)$_4$ was 0.69 eV, and the relative HOMO offsets (Δ E_{HOMO}) was 0.37 eV, both of which are large enough to guarantee efficient exciton dissociation [37]. The difference between the LUMO of BP(DPPB)$_4$ and the HOMO of P3HT was as large as 1.31 eV, which may result in PSCs with a high V_{oc}.

Morphology

The morphology of the blend film was characterized by transmission electron microscopy (TEM). The TEM images (Fig. 5) of as-cast devices do not show obvious D–A phase separation (Fig. 5a). When the devices were annealed by

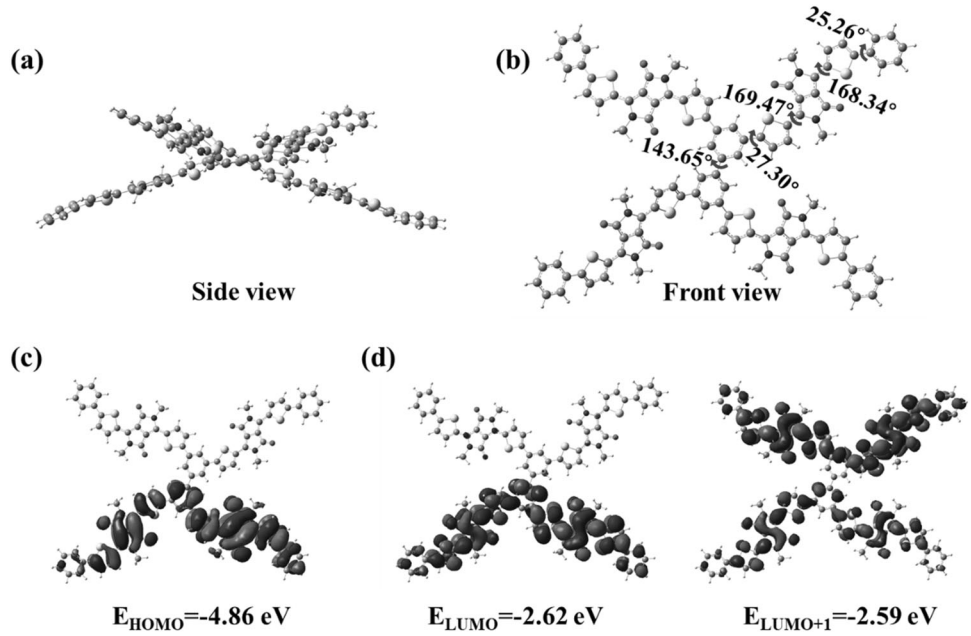

Fig. 3 Local optimized geometries and frontier molecular orbital distributions of $BP(DPPB)_4$

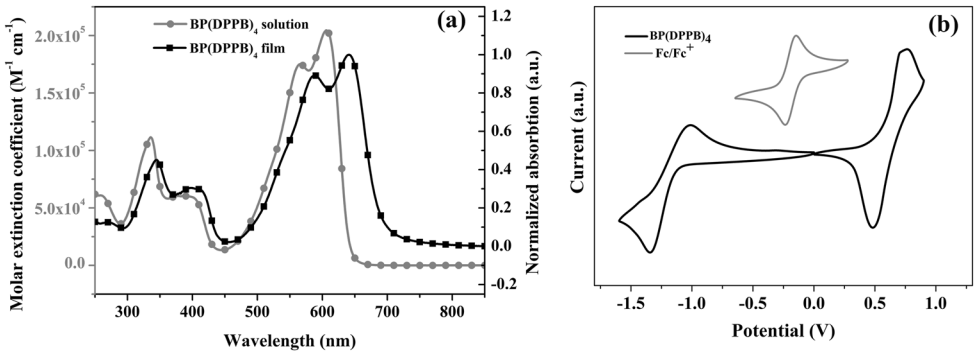

Fig. 4 **a** Absorption spectra of $BP(DPPB)_4$ in film and solution; **b** CV curve of $BP(DPPB)_4$

Table 1 Optical and electrochemical properties of $BP(DPPB)_4$

	λ_{film} (nm)	$\lambda_{solution}$ (nm)	λ_{onset} (nm)	$E_g^{opt\ a}$ (eV)	E_{LUMO}^{b} (eV)	E_{HOMO}^{b} (eV)
$BP(DPPB)_4$	589,641	565,607	693	1.79	−3.63	−5.31
P3HT	542,595	—	639	1.94	−2.94 [36]	−4.94 [36]

[a]Calculated by $1240/\lambda_{onset}$; [b]estimated from cyclic voltammetry

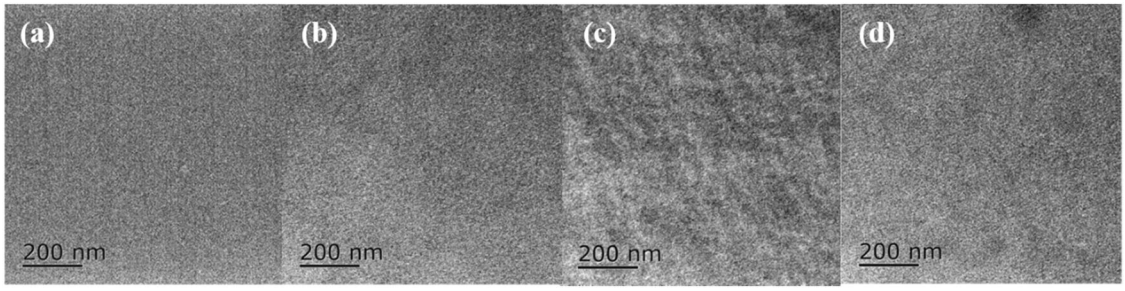

Fig. 5 TEM images of P3HT:$BP(DPPB)_4$ blend films that are **a** as cast; **b** thermally annealed at 80 °C for 10 min; **c** thermally annealed at 120 °C for 10 min; and **d** thermally annealed at 150 °C for 10 min

thermal annealing at 80 °C for 10 min, slightly interpenetrating structures and phase separation appeared (Fig. 5b). As shown in Fig. 5c, upon thermal annealing at 120 °C for 10 min, obvious nanoscale interpenetrating structures and improved phase separation between the donor and acceptor formed. This morphology would lead to more-efficient exciton dissociation and charge transfer and result in higher J_{sc} and FF values for annealed devices. However, when the thermal annealing temperature was increased to 150 °C, the nanoscale structures disappeared, and phase separation decreased, as shown in Fig. 5d. This effect possibly would result in lower J_{sc} and FF values. Clearly, the results are closely associated with the DSC results. Because the glass transition temperature (T_g) of BP(DPPB)$_4$ is 120 °C, when the annealing temperature reaches 120 °C, BP(DPPB)$_4$ is able to further self-aggregate, resulting in good morphology with obvious nanoscale interpenetrating structures and appropriate phase separation [38, 39]. However, when the annealing temperature is higher than the T_g of BP(DPPB)$_4$ at 150 °C, BP(DPPB)$_4$ diffuses into the P3HT matrix, resulting in inconspicuous phase separation between the donor and acceptor.

Photovoltaic performance

Because the absorption spectrum and the energy levels of BP(DPPB)$_4$ matched well with those of P3HT, P3HT and BP(DPPB)$_4$ were used as the electron donor and electron acceptor, respectively, to fabricate PSCs. The structure of the PSCs was ITO/PEDOT:PSS/P3HT:BP(DPPB)$_4$/Ca/Al with a donor:acceptor weight ratio of 2:1. Different annealing temperatures are assessed to optimize device performance. Figure 6a shows the *J*–*V*) characteristics of the PSCs under AM 1.5G illumination at an intensity of 100 mW cm^{-2}, and all photovoltaic data are summarized in Table 2. Thermal annealing can significantly improve device performance. A low PCE of 0.35% with a V_{oc} of 1.19 V, a J_{sc} of 1.15 mA cm^{-2}, and an FF of 0.25 was obtained for the as-cast devices. When there was thermal annealing and the temperature increased to 80 °C, the photovoltaic performance improved sharply to a PCE of 0.83% with a V_{oc} of 1.19 V, a J_{sc} of 2.43 mA cm^{-2}, and an FF of 0.29.

Furthermore, upon thermal annealing at 120 °C for 10 min, the device could reach a maximum PCE of 1.43% with a V_{oc} of 1.17 V, a J_{sc} of 3.41 mA cm^{-2}, and an FF of 0.36, which is consistent with previous reports in the literature [21–28, 40–42] (Supporting information Table S2 and Scheme S1). However, when the thermal annealing temperature was further increased to 150 °C, the performance decreased notably, with a PCE of 0.61%, a V_{oc} of 1.12 V, a J_{sc} of 1.53 mA cm^{-2}, and an FF of 0.36. Apparently, thermal annealing significantly improves the J_{sc} and FF, thereby further improving device performance. In addition, the enhanced photovoltaic performance of the device that was thermally annealed at 120 °C for 10 min should also be ascribed to the lower series resistance (R_s) of 3992.90 ohm because of the interpenetrating network in the active layer, as proved by the TEM results, and the higher shunt resistance (R_{sh}) of 17373.48 ohm, indicating reduced leakage current.

The photoresponses of PSCs based on P3HT:BP(DPPB)$_4$ with or without thermal annealing at 120 °C for 10 min were investigated by determining the external quantum efficiency (EQE) covering the wavelength range from 300 to 800 nm. As shown in Fig. 6b, the EQE curves of the two PSCs showed a similar broad range from 300 nm to 720 nm. It is obvious that the EQE value of the annealed devices is 4 times higher than that of the as-cast device. The maximum EQE of the annealed devices reached 20% at 520 nm, which is in agreement with the variations in J_{sc} values in the

Table 2 Summary of photovoltaic performance of PSCs based on P3HT:BP(DPPB)$_4$ after thermal annealing at different temperatures (D:A = 2:1)

Annealing	V_{oc} (V)	J_{sc} (mA cm^{-2})	FF (%)	PCE (%)	R_s ohm	R_{sh} ohm
Without	1.19	1.15	0.25	0.35	21,310.73	24,448.26
80 °C	1.19	2.43	0.29	0.83	6817.42	14,404.66
120 °C	1.17	3.41	0.36	1.43	3992.90	17,373.48
150 °C	1.12	1.53	0.36	0.61	8013.93	33,838.66

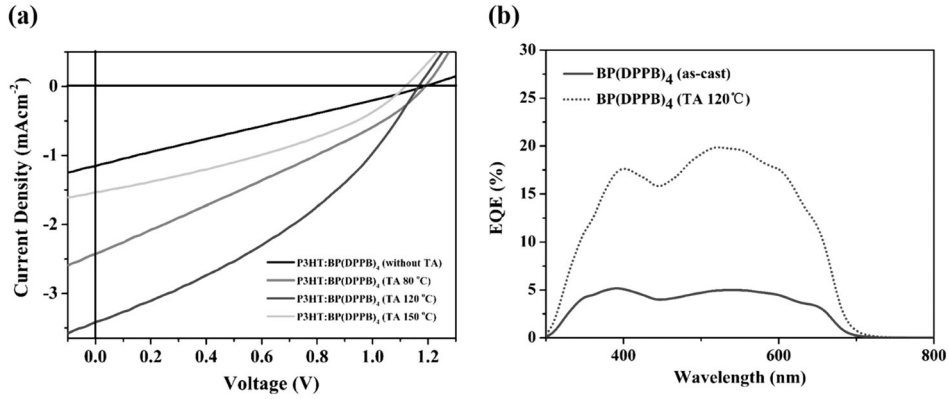

Fig. 6 **a** *JV* characteristics of solar cells based on P3HT:BP(DPPB)$_4$ (D:A = 2:1) with different thermal annealing temperatures; photocurrent density versus effective voltage characteristics of **b** EQE curves of solar cells based on P3HT:BP(DPPB)$_4$

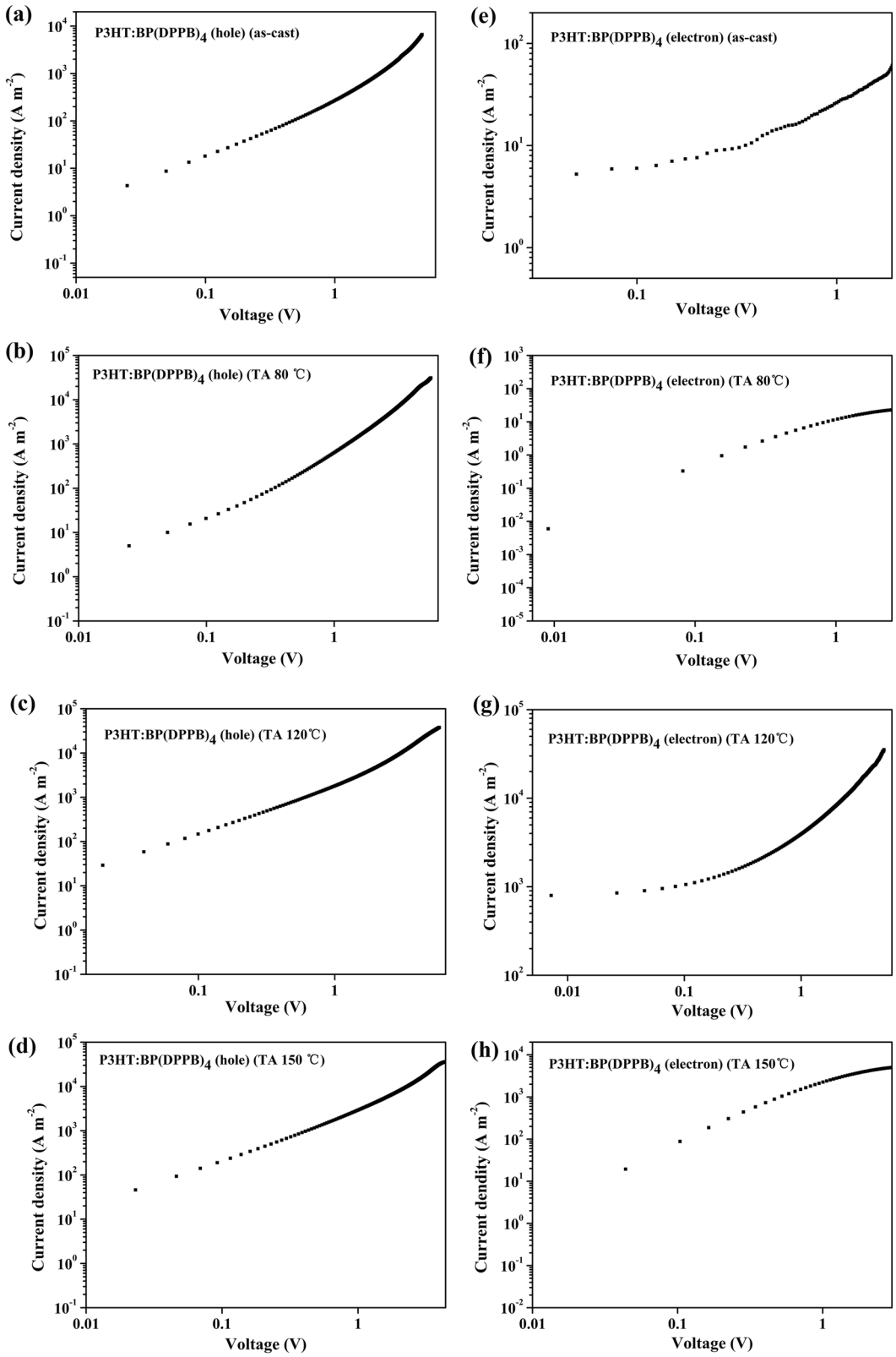

Fig. 7 $J^{1/2}$–V curves for hole-only (the first line) and electron-only (the second line) devices based on 2:1 P3HT:BP(DPPB)$_4$ films subjected to different thermal annealing temperatures: **a**, **e** as-cast; **b**, **f** thermal annealing at 80 °C; **c**, **g** thermal annealing at 120 °C; and **d**, **h** thermal annealing at 150 °C. All of the samples were maintained at the corresponding temperatures for 10 min

devices. We also used the SCLC method to measure the charge carrier mobility in order to investigate the electron transport properties of the devices. Figure 7 shows the dark *J*–*V* curves of the hole-only and electron-only devices after thermal annealing at different temperatures, and all data are summarized in Table 3. It is clear that thermal annealing promotes the charge carrier mobility. The as-cast devices provided the lowest hole and electron mobility. As the annealing temperature increased, the charge carrier mobility increased. When the annealing temperature increased to 120 °C, the highest hole and electron mobility of the blend film were calculated to be 4.83×10^{-4} cm^2 V^{-1} s^{-1} and 2.45×10^{-4} cm^2 V^{-1} s^{-1}, respectively. However, when the thermal annealing temperature was further increased to 150 °C, the charge carrier mobility decreased, which is consistent with the trend in the PCE values of the devices. In addition, the charge carrier mobility data in this work are comparable with the data reported by other research groups, as listed in Table 4. Thus, the charge carrier mobility values are appropriate and believable. Compared with those without thermal annealing and those subjected to different annealing temperatures, devices after thermal annealing at 120 °C for 10 min showed more balanced hole/electron transport in the active layer, which may account for the relatively higher FF.

Table 3 Charge carrier mobilities of devices based on P3HT:BP(DPPB)$_4$ films

Acceptors	μ_e (cm^2 V^{-1} s^{-1})	μ_h (cm^2 V^{-1} s^{-1})	μ_h/μ_e
As-cast	4.59×10^{-6}	1.56×10^{-5}	4.00
TA 80 °C	2.16×10^{-5}	7.57×10^{-5}	3.50
TA 120 °C	2.45×10^{-4}	4.83×10^{-4}	1.97
TA 150 °C	7.43×10^{-5}	2.88×10^{-4}	3.88

Table 4 Charge carrier mobilities of small-molecule acceptors based on DPP units

Acceptors	μ_e[a] (cm^2 V^{-1} s^{-1})	μ_h[a] (cm^2 V^{-1} s^{-1})	ref.
TFPDPP	–	–	[21]
DPP-TA1	3×10^{-3}(O,N)	–	[22]
N6	–	–	[23]
DPP1	8×10^{-6}(O,N)	–	[24]
DBS-2DPP	2.8×10^{-5}(S,B)	6.1×10^{-4}(S,B)	[40]
F(DPP)$_2$B$_2$	–	–	[41]
S(TPA-DPP)	6.8×10^{-6}(S,B)	2.8×10^{-4}(S,B)	[25]
SF-DPPEH	–	–	[26]
SF(DPPB)$_4$	1.3×10^{-4}(S,B)	1.48×10^{-4}(S,B)	[27]
SF(DPPFB)$_4$	2.9×10^{-4}(S,B)	1.6×10^{-4}(S,B)	[42]
SF-(DPP3F)$_4$	–	–	[28]
BP(DPPB)$_4$	2.45×10^{-4}(S,B)	4.83×10^{-4}(S,B)	This work

[a]O and S: measured by OTFT or the space-charge-limited current (SCLC) method; N and B: in a neat or blend film

Conclusion

A new nonfullerene electron acceptor, BP(DPPB)$_4$, with a diphenyl core and four diketopyrrolopyrrole arms was designed, synthesized, and characterized. BP(DPPB)$_4$ shows appropriate absorption bands and matched energy levels with P3HT. Moreover, PSCs based on P3HT and BP(DPPB)$_4$ blend films can achieve a moderate PCE of 1.43% with an outstandingly high V_{oc} of 1.17 V after thermal annealing at 120 °C for 10 min. These results demonstrate that the BP unit is a useful fragment to construct multi-dimensional NFAs and that BP(DPPB)$_4$ is a promising NFA for future practical applications in PSCs.

Acknowledgements This work was supported by the National Natural Science Foundation of China (NSFC 51703172, 21702154, and 51773157), the Wuhan Yellow Crane Program for Excellent Talents, the Hubei Technology Innovation Major Project (2016AAA030), the Foundation for Outstanding Youth Innovative Research Groups of Higher Education Institution in Hubei Province (T201706), the Foundation for Innovative Research Groups of Hubei Natural Science Foundation of China (2017CFA009), the Natural Science Foundation of Hubei (ZRMS2017001), and the Science Foundation of Wuhan Institute of Technology (k201629).

Compliance with ethical standards

Conflict of interest The authors declare that they have no conflict of interest.

Publisher's note: Springer Nature remains neutral with regard to jurisdictional claims in published maps and institutional affiliations.

References

1. Li Y. Molecular design of photovoltaic materials for polymer solar cells: toward suitable electronic energy levels and broad absorption. Acc Chem Res. 2012;45:723–33.
2. Duan C, Huang F, Cao Y. Recent development of push–pull conjugated polymers for bulk-heterojunction photovoltaics: rational design and fine tailoring of molecular structures. J Mater Chem. 2012;22:10416–34.
3. Li H, Xiao Z, Ding L, Wang J. Thermostable single-junction organic solar cells with a power conversion efficiency of 14.62%. Sci Bull. 2018;63:340–2.
4. Cui Y, Yao H, Hong L, Zhang T, Xu Y, Xian K, et al. Achieving over 15% efficiency in organic photovoltaic cells via copolymer design. Adv Mater. 2019;31:1808356.
5. Liu Y, Mu C, Jiang K, Zhao J, Li Y, Zhang L, et al. A tetraphenylethylene core-based 3d structure small molecular acceptor enabling efficient non-fullerene organic solar cells. Adv Mater. 2015;27:1015–20.
6. Mihailetchi VD, van Duren JKJ, Blom PWM, Hummelen JC, Janssen RAJ, Kroon JM, et al. Electron transport in a methanofullerene. Adv Funct Mater. 2003;13:43–46.
7. Zhao J, Li Y, Lin H, Liu Y, Jiang K, Mu C, et al. High-efficiency non-fullerene organic solar cells enabled by a difluorobenzothiadiazole-based donor polymer combined with a properly matched small molecule acceptor. Energ Environ Sci. 2015;8:520–5.

8. Li CZ, Yip HL, Jen AKY. Functional fullerenes for organic photovoltaics. J Mater Chem. 2012;22:4161–77.
9. Nielsen CB, Holliday S, Chen HY, Cryer SJ, McCulloch I. Non-fullerene electron acceptors for use in organic solar cells. Acc Chem Res. 2015;48:2803–12.
10. Zhan C, Yao J. More than conformational "twisting" or "coplanarity": molecular strategies for designing high-efficiency non-fullerene organic solar cells. Chem Mater. 2016;28:1948–64.
11. Gao L, Zhang ZG, Xue L, Min J, Zhang J, Wei Z, et al. All-polymer solar cells based on absorption-complementary polymer donor and acceptor with high power conversion efficiency of 8.27%. Adv Mater. 2016;28:1884–90.
12. Li S, Zhang H, Zhao W, Ye L, Yao H, Yang B, et al. Green-solvent-processed all-polymer solar cells containing a perylene diimide-based acceptor with an efficiency over 6.5%. Adv Energy Mater. 2016;6:1501991.
13. Nakashima M, Otsura T, Naito H, Ohshita J. Synthesis of new D-A polymers containing disilanobithiophene donor and application to bulk heterojunction polymer solar cells. Polym J. 2015;47:733–8.
14. Mori H, Nishihara Y. Low-bandgap semiconducting polymers based on sulfur-containing phenacene-type molecules for transistor and solar cell applications. Polym J. 2018;50:615–25.
15. Liu Z, Zhang L, Shao M, Wu Y, Zeng D, Cai X, et al. Fine-tuning the quasi-3d geometry: enabling efficient nonfullerene organic solar cells based on perylene diimides. Acs Appl Mater Inter. 2018;10:762–8.
16. Liu Z, Zhang L, Gao X, Zhang Q, Shi S. Synthesis and characterization of novel red-emitting conjugated polymers based on triphenylaminesilole-carbazole-fluorene. Mater Chem Phys. 2018;212:208–13.
17. Gao X, Shen J, Chen B, Liu Z, Zhang Q. Synthesis and characterization of conjugated polymers containing bromide side chain. J Mater Sci Mater Electron. 2017;28:18049–56.
18. Qu S, Tian H. Diketopyrrolopyrrole (DPP)-based materials for organic photovoltaics. Chem Commun. 2012;48:3039–51.
19. Bronstein H, Chen Z, Ashraf RS, Zhang W, Du J, Durrant JR, et al. Thieno[3,2-b]thiophene−diketopyrrolopyrrole-containing polymers for high-performance organic field-effect transistors and organic photovoltaic devices. J Am Chem Soc. 2011;133:3272–5.
20. Maruo H, Sasaki Y, Harada K, Suwa K, Oyaizu K, Segawa H, et al. Hole-transporting diketopyrrolopyrrole-thiophene polymers and their additive-free application for a perovskite-type solar cell with an efficiency of 16.3%. Polym J. 2019;51:91–96.
21. Sonar P, Ng GM, Lin TT, Dodabalapur A, Chen ZK. Solution processable low bandgap diketopyrrolopyrrole (dpp) based derivatives: novel acceptors for organic solar cells. J Mater Chem. 2010;20:3626–36.
22. Karsten BP, Bijleveld JC, Janssen RAJ. Diketopyrrolopyrroles as acceptor materials in organic photovoltaics. Macromol Rapid Commun. 2010;31:1554–9.
23. Raynor AM, Gupta A, Patil H, Bilic A, Bhosale SV. A diketopyrrolopyrrole and benzothiadiazole based small molecule electron acceptor: design, synthesis, characterization and photovoltaic properties. RSC Adv. 2014;4:57635–8.
24. Patil H, Zu WX, Gupta A, Chellappan V, Bilic A, Sonar P, et al. A non-fullerene electron acceptor based on fluorene and diketopyrrolopyrrole building blocks for solution-processable organic solar cells with an impressive open-circuit voltage. Phys Chem Chem Phys. 2014;16:23837–42.
25. Lin Y, Cheng P, Li Y, Zhan X. A 3D star-shaped non-fullerene acceptor for solution-processed organic solar cells with a high open-circuit voltage of 1.18 V. Chem Commun. 2012;48:4773–5.
26. Wu X, Fu W, Xu Z, Shi M, Liu F, Chen H, et al. Spiro linkage as an alternative strategy for promising nonfullerene acceptors in organic solar cells. Adv Funct Mater. 2015;25:5954–66.
27. Li S, Liu W, Shi M, Mai J, Lau TK, Wan J, et al. A spirobifluorene and diketopyrrolopyrrole moieties based non-fullerene acceptor for efficient and thermally stable polymer solar cells with high open-circuit voltage. Energ Environ Sci. 2016;9:604–10.
28. Chen Z, Xie Y, Yu Y, Wu H, Wan J. A comparative study of the effects of terminal aromatic moieties in spirobifluorene core-based diketopyrrolopyrrole non-fullerene acceptors. New J Chem. 2018;42:11854–61.
29. Liu Z, Wu Y, Jiang H, Zhang L, Zeng D, Zhang X, et al. A new nonfullerene acceptor based on perylene diimides for organic solar cells. J Mater Sci, Mater Electron. 2018;29:10362–8.
30. Shin W, Yasuda T, Hidaka Y, Watanabe G, Arai R, Nasu K, et al. π-extended narrow-bandgap diketopyrrolopyrrole-based oligomers for solution-processed inverted organic solar cells. Adv Energy Mater. 2014;4:1400879.
31. Pan J, Zuo L, Hu X, Fu W, Chen M, Fu L, et al. Star-shaped D–A small molecules based on diketopyrrolopyrrole and triphenylamine for efficient solution-processed organic solar cells. Acs Appl Mater Inter. 2013;5:972–80.
32. Lee NJ, Lee DH, Kim DW, Lee JH, Cho SH, Jeon WS, et al. Highly efficient soluble materials for blue phosphorescent organic light–emitting diode. Dyes Pigments. 2012;95:221–8.
33. Zhang G, Zhao J, Chow PCY, Jiang K, Zhang J, Zhu Z, et al. Nonfullerene Acceptor Molecules for Bulk Heterojunction Organic Solar Cells. Chem Rev. 2018;118:3447–507.
34. Ma H, Troisi A. Modulating the exciton dissociation rate by up to more than two orders of magnitude by controlling the alignment of LUMO+1 in organic photovoltaics. J Phys Chem C. 2014;118:27272–80.
35. Kuzmich A, Padula D, Ma H, Troisi A. Trends in the electronic and geometric structure of non-fullerene based acceptors for organic solar cells. Energ Environ Sci. 2017;10:395–401.
36. Jiang B, Zhang X, Zhan C, Lu Z, Huang J, Ding X, et al. Benzodithiophene bridged dimeric perylene diimide amphiphiles as efficient solution-processed non-fullerene small molecules. Polym Chem. 2013;4:4631–8.
37. Brabec CJ, Winder C, Sariciftci NS, Hummelen JC, Dhanabalan A, van Hal PA, et al. A low-bandgap semiconducting polymer for photovoltaic devices and infrared emitting diodes. Adv Funct Mater. 2002;12:709–12.
38. Chang SC, Hsiao YJ, Li TS. Selecting annealing temperature of P3HT/PCBM incorporated with nano-diamonds using thermal desorption spectroscopy. Int J Electrochem Sc. 2015;10:1658–68.
39. Zhang Y, Parnell AJ, Pontecchiani F, Cooper JFK, Thompson RL, Jones RAL, et al. Understanding and controlling morphology evolution via DIO plasticization in PffBT4T/PC71BM devices. Sci Rep-Uk. 2017;7:44269.
40. Lin Y, Li Y, Zhan X. A solution-processable electron acceptor based on dibenzosilole and diketopyrrolopyrrole for organic solar cells. Adv Energy Mater. 2013;3:724–8.
41. Shi H, Fu W, Shi M, Ling J, Chen H. A solution-processable bipolar diketopyrrolopyrrole molecule used as both electron donor and acceptor for efficient organic. J Mater Chem A. 2015;3:1902–5.
42. Yuan C, Liu W, Shi M, Ling S, Wang Y, Chen H, et al. A non-fullerene electron acceptor with a spirobifluorene core and four diketopyrrolopyrrole arms end capped by 4-fluorobenzene. Dyes Pigments. 2017;143:217–22.